

## PECVD Processing of low bandgap-energy amorphous hydrogenated germanium-tin (a-GeSn:H) films for opto-electronic applications

de Vrijer, Thierry; Roodenburg, Koos; Saitta, Federica; Blackstone, Thijs; Limodio, Gianluca; Smets, Arno H.M.

**DOI**

[10.1016/j.apmt.2022.101450](https://doi.org/10.1016/j.apmt.2022.101450)

**Publication date**

2022

**Document Version**

Final published version

**Published in**

Applied Materials Today

**Citation (APA)**

de Vrijer, T., Roodenburg, K., Saitta, F., Blackstone, T., Limodio, G., & Smets, A. H. M. (2022). PECVD Processing of low bandgap-energy amorphous hydrogenated germanium-tin (a-GeSn:H) films for opto-electronic applications. *Applied Materials Today*, 27, 1-9. Article 101450. <https://doi.org/10.1016/j.apmt.2022.101450>

**Important note**

To cite this publication, please use the final published version (if applicable). Please check the document version above.

**Copyright**

Other than for strictly personal use, it is not permitted to download, forward or distribute the text or part of it, without the consent of the author(s) and/or copyright holder(s), unless the work is under an open content license such as Creative Commons.

**Takedown policy**

Please contact us and provide details if you believe this document breaches copyrights. We will remove access to the work immediately and investigate your claim.



# PECVD Processing of low bandgap-energy amorphous hydrogenated germanium-tin (a-GeSn:H) films for opto-electronic applications

Thierry de Vrijer\*, Koos Roodenburg, Federica Saitta, Thijs Blackstone, Gianluca Limodio, Arno H.M. Smets

Photovoltaic Materials and Devices, TU Delft, Mekelweg 4, Delft 2628CD, The Netherlands

## ARTICLE INFO

### Article history:

Received 13 January 2022

Revised 3 March 2022

Accepted 15 March 2022

### Keywords:

Plasma enhanced chemical vapour deposition

Amorphous films

Low bandgap energy

Hydrogenated germanium Ge:H

Germanium-tin GeSn

## ABSTRACT

An alloy based on the group IV elements germanium and tin has the potential of yielding an earth-abundant low bandgap energy semiconductor material with applications in the fields of micro-electronics, optics, photonics and photovoltaics. In this work, the first steps towards the plasma enhanced chemical vapour deposition (PECVD) processing of a chemically stable, low bandgap energy and intrinsic GeSn:H alloy are presented. Using a tetramethyltin (TMT) precursor, over 70 PECVD processed films are presented. It was observed that the opto-electrical film properties are a result of the material phase fraction, void fraction, hydrogenation and the level of tin and carbon integration. In particular, managing the carbon integration from the TMT precursor into the material is crucial for obtaining low-bandgap and chemically stable materials. The collective findings from this work will aid in successfully identifying PECVD processing pathways for GeSn:H.

© 2022 The Author(s). Published by Elsevier Ltd.

This is an open access article under the CC BY license (<http://creativecommons.org/licenses/by/4.0/>)

## 1. Introduction

An alloy based on the group IV elements germanium and tin has the potential of yielding a relatively earth-abundant and safe semiconductor material with a low bandgap energy. Such a GeSn alloy has potential applications in general CMOS compatible optical devices [1], for use in a mid-infrared laser [2] or light-emitting diodes [3,4]. Alternatively, research is performed on (Si)GeSn to develop a lattice matched direct bandgap option for III-V semiconductor based photovoltaic multijunction devices [5–7]. The far majority of works consider the epitaxial growth of GeSn films. For epitaxial film growth, deposition techniques such as molecular beam epitaxy [8–11], co-evaporation [12], and sputtering [13,14] are used, as well as chemical vapour deposition (CVD) at reduced pressure [3,15–17], low pressure [7] and ultra-high vacuum [4,18,19].

Only a small number of works have explored the use of amorphous (a-)GeSn. These a-GeSn films were sputtered [20–22] or evaporated [23], but the use of CVD for a-GeSn films has not yet been reported. Using a CVD processing technique, such as plasma-enhanced CVD (PECVD), would potentially allow for the relatively cheap and fast processing of a-GeSn films and is compatible with

the conventional and mature processing techniques used for the processing of thin film silicon alloys for photovoltaic and display applications. For that reason, in this work, a first investigation is performed on the PECVD processing of hydrogenated (:H) a-GeSn. The purpose of such an amorphous hydrogenated alloy would not be to provide a cheaper alternative for the processing of epitaxially grown GeSn, but rather to explore a low-cost industry-compatible group IV alloy for PV applications, and potential additional applications in the fields of micro-electronics, optics and photonics. To successfully identify PECVD processing pathways for a-GeSn:H, the advantages, challenges and limitations are evaluated using vibrational- and elemental spectroscopy, spectroscopic ellipsometry and electrical characterization techniques.

## 2. Experimental section

For the development of the GeSn:H films, a tin precursor is added during the growth of the hydrogenated germanium films. The processing conditions of the Ge:H films were optimized in our earlier work [24–26]. The typical deposition conditions for nc-Ge:H and a-Ge:H films used in this work are presented in Table 1. Generally, for the PECVD processing of hydrogenated amorphous alloys, a precursor such as methane [CH<sub>4</sub>], silane [SiH<sub>4</sub>] or germane [GeH<sub>4</sub>] is used, where the desired element is bonded to 4 hydrogen atoms. Such a SnH<sub>4</sub> precursor is not chemically stable however. Some works report the use of in-house developed

\* Corresponding author.

E-mail address: [t.devrijer@tudelft.nl](mailto:t.devrijer@tudelft.nl) (T. de Vrijer).

deuter-ostannane [SnD<sub>4</sub>] as a Sn-precursor [4,19], which uses the hydrogen isotope deuterium to improve the stability of the precursor. Others report the use of the commercially available SnCl<sub>4</sub> [7], tetra-ethyltin [Sn(C<sub>2</sub>H<sub>5</sub>)<sub>4</sub>] [27,28] and tetra-methyltin [Sn(CH<sub>3</sub>)<sub>4</sub>] (TMT) [16]. In this work TMT is used, as it is the least complex, commercially available Sn-precursor that exclusively consists of group IV elements and hydrogen. A challenge with this precursor is that four CH<sub>3</sub> groups are introduced into the reactor with each Sn-atom. Carbon integration is generally undesirable, as it results in an increase of the bandgap energy [26,29,30], an effect opposite to that of Sn-integration.

The GeSn:H films are batch-processed on different substrates simultaneously. Quartered 500μm monocrystalline silicon wafers of 4 inch size are used for Fourier Transform Infrared (FTIR) spectroscopy, Raman spectroscopy (Raman), Energy Dispersive X-Ray Spectroscopy (EDX) and Scanning Electron Microscopy (SEM) analysis. Corning Eagle XG glass substrates of 10cm x 2.5cm are used for all other measurements. The GeSn:H films were processed in the Cascade radiofrequency-PECVD reactor, which has a circular electrode with a diameter of 160mm. Cascade is a laminar flow reactor, where germane (GeH<sub>4</sub>), molecular hydrogen and TMT are used as precursor gasses. The TMT, a liquid at room temperature, is evaporated in a separate canister at 70 °C. Injection of TMT into the reactor is controlled through a valve, similar to those used for atomic layer deposition. For the samples presented in this work, the open time of the valve was varied between 5-10ms while the close time was varied between 100ms and 60s. The ratio of the close time to the open time is referred to as the duty cycle ( $\delta$ ). For a fraction of the GeSn:H samples the TMT flow from the canister, prior to injection into the reactor, was diluted in Helium. Considering the relatively high duty cycles used in this work, the impact of He dilution on the plasma is assumed to be minimal. He dilution mainly serves to decrease the TMT concentration introduced during each injection event.

It should be noted that for the samples with the largest duty cycles, the close time is expected to exceed the residence time of the injected TMT. The residence time ( $\tau$ ) can be calculated according to eq.1, where  $V_R$  is the reactor volume,  $p$  the pressure during deposition,  $T$  the temperature of the precursor gas.  $F_{gas}$  is the cumulative gas flow rate in sccm,  $p_0$  the standard pressure of 1.01bar and  $T_0$  the standard temperature of 273K. With  $V_R \approx 10L$ ,  $T \approx 300K$ ,  $p=4mbar$  and  $F_{gas} \approx 200sccm$ , the residence time is on the order of 10s, while the close time of the valve is increased up to 60s.

$$\tau = \frac{V_R p T_0}{F_{gas} p_0 T} \quad (1)$$

The methods for obtaining the activation energy ( $E_{act}$ ), the dark conductivity at room temperature  $\sigma_d$  and photoconductivity  $\sigma_{ph}$  are similar to those used in earlier work [24,25]. Spectroscopic Ellipsometry (SE) was used to determine the refractive index at a wavelength of 600nm ( $n_{@600nm}$ ), as well as the thickness and optical bandgap energy  $E_{04}$ , which is the energy at which the absorption coefficient of the film equals  $10^4 cm^{-1}$ . The SE measurements were fitted using a Cody-Lorentz model, which provides excellent representation of the processed materials.

A Thermo Fisher Nicolet 5700 spectrometer and an inVia confocal Raman microscope were used to obtain the FTIR- and Raman spectra. Additionally, SEM and EDX analysis was performed on a FEI Nova NanoSEM 450. SEM imaging was performed at an acceleration voltage of 10kV, while EDX measurements were performed at 5KV. The FTIR, Raman and EDX spectra were fitted using the Fityk freeware [31]. The background was subtracted manually. Examples of Raman and FTIR spectra, typical for chemically stable GeSn:H samples with low oxygen content, including the identification of peaks relevant for the characterisation performed in this work, are presented in Fig. 1. Peak identification is performed based on an

extensive study of the vibrational spectra of hydrogenated group IV alloys presented in [32]. Additional FTIR spectra, typical for samples suffering from post-deposition oxidation, can be found in the supplementary information.

Examples of typical EDX spectra are provided in the main text. The elemental composition was obtained by comparing the area of fitted Gaussian distributions after background subtraction. As such, the elemental fractions represent atomic fractions ( $at_x$ ) rather than weight fractions. Atomic fractions of oxygen present in the material are not intentionally added during deposition, but are the results of post-deposition oxidation and indicative of a chemically unstable material. The Raman spectroscopy measurements were used to determine the crystallinity ( $\chi_c$ ). The method for determining crystallinity is reported elsewhere [24].

In addition to the atomic fractions and the crystallinity, the relative number of hydrogen atoms ( $N_H$ ) bonded to germanium and carbon was determined from the absorbance peaks in the FTIR spectra, using:

$$N_H = A \cdot \frac{A_{abs}(\omega)}{d} \ln(10) \cdot \omega^{-1} \quad (2)$$

Here  $\omega$  is the wavenumber,  $d$  the thickness of the films,  $A_{abs}$  the area of the Gaussian distribution corresponding to Ge-H or C-H vibrations, respectively.  $A$  is an empirically determined proportionality constant that is different for the C-H and Ge-H vibrations, as it is a function of the effective charge, mass and frequency of the dipole [33]. For determining the number of hydrogen atoms bonded to germanium ( $N_{H-Ge}$ ), the Ge-H wagging modes, positioned at around  $560 cm^{-1}$ , are conventionally used, as the strength of the wagging modes is proportional to the hydrogen concentration, while the strength of the stretching modes is not [34]. For the Ge-H wagging mode, a proportionality constant of  $A=1.3 \cdot 10^{19} cm^{-2}$  is used, as determined by [35] and in line with the  $1.1 \cdot 10^{19} cm^{-2}$  used by [34]. For determining the number of hydrogen atoms bonded to carbon ( $N_{H-C}$ ). The C-H stretching modes are conventionally used [36–39]. This is presumably because C-H wagging occurs in a region generally occupied by a large number of vibrational modes, as demonstrated in [32], making deconvolution of different absorbance-peaks challenging and arbitrary. For the C-H stretching modes, a proportionality constant of  $A=1.35 \cdot 10^{21} cm^{-2}$  is used, similar to [36,37] and in the same order as the value of  $1.7 \cdot 10^{21} cm^{-1}$  used by [38,39]. Finally, the ratio between the hydrogen atoms bonded to carbon and germanium ( $R_{CH/GeH}$ ) was determined using:

$$R_{CH/GeH} = \frac{N_{H-C}}{N_{H-C} + N_{H-Ge}} \quad (3)$$

### 3. Results and discussion

#### 3.0.1. Introducing TMT

For a first experiment, TMT is injected into the reactor at various duty cycles during a-Ge:H deposition, using the conditions reported in Table 1. This initial exploration revealed certain inherent challenges to the processing of GeSn:H using TMT, specifically at relatively low duty cycles of approximately  $\delta < 1000$ . The first is indicated by the SEM images in Fig. 2, where an inhomogeneous distribution of Sn can be observed at different magnifications. In the top left image, distribution of Sn across a diagonal over the sample surface can be observed, believed to be following a path from the TMT injector to the turbopump. An artifact therefore of the laminar-flow-design of the reactor. The second challenge can be observed in Fig. 3, where in the top-left image the formation of Sn clusters on the sample surface can be observed. This observation is in line with earlier reports, where the clustering of Sn for epitaxially grown GeSn was observed for deposition temperatures over 200–230 °C[9,10].

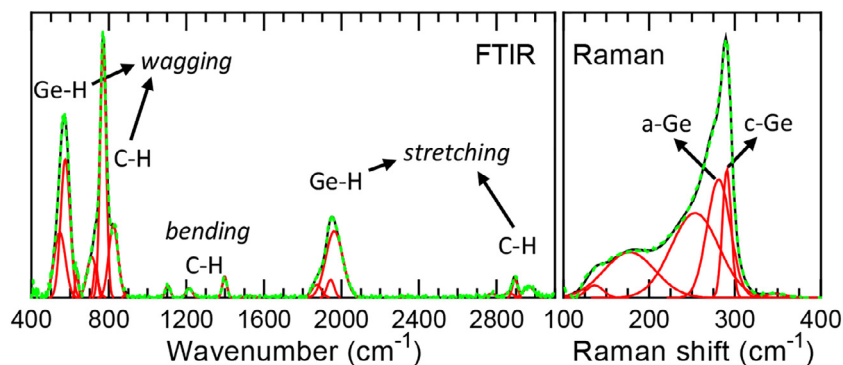


**Fig. 1.** Typical FTIR (left) and Raman (right) spectra of un-oxidized GeSn:H films. Raman spectrum is of an nc-GeSn:H film. The individual fitted Gaussian's (red), sum of the fitted Gaussian's (black) and measurements after background subtraction (green, dashed) are shown. The amorphous and crystalline Ge vibrational modes are indicated in the Raman plot, while the Ge-H and C-H vibrational modes are indicated in the FTIR plot. (For interpretation of the references to colour in this figure legend, the reader is referred to the web version of this article.)

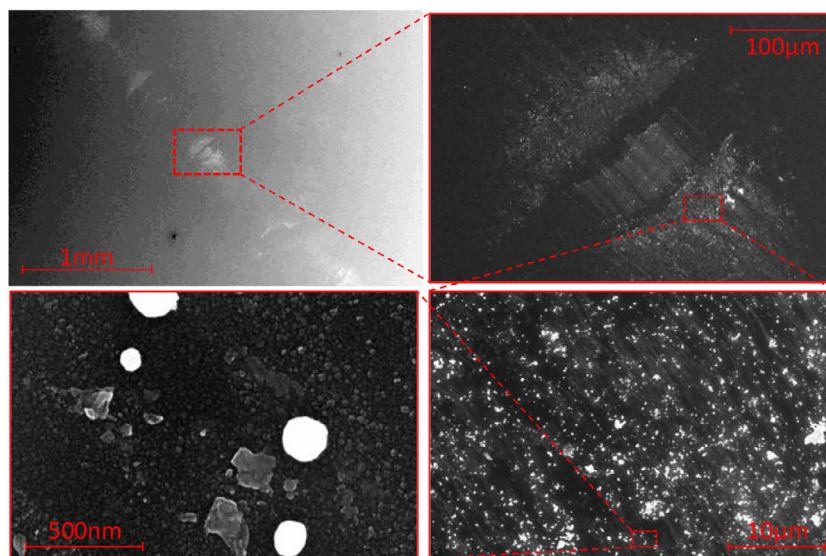


**Fig. 2.** Four SEM images at different magnification of the surface of an a-GeSn:H sample with  $\delta=100$  and  $F_{He}=0\text{scm}$ .

In an attempt to prevent the clustering of Sn and distribute the TMT more evenly, the evaporated TMT was diluted in Helium in the canister prior to insertion into the reaction chamber. It can be observed, in the top-right image in Fig. 3, that the He-dilution, for the very low  $\delta=100$ , does not prevent the clustering of Sn but rather results in a change of geometry of the Sn-clusters. The EDX plot in Fig. 3 demonstrates that the formations on the sample surface are indeed Sn clusters. These two challenges, related to the inhomogeneous distribution of TMT in a laminar flow reactor and the clustering of Sn at elevated deposition temperature, were exclusively observed in SEM images for relatively low  $\delta$ . As such, these challenges could be considered boundary conditions for the processing of GeSn with this particular Sn-precursors and reactor design. Additionally, relatively high carbon and oxygen contents can be observed in the EDX plot of Fig. 3, for the position on the surface measured next to the Sn cluster (blue circle). As indicated in Section 2, with the TMT precursor four  $\text{CH}_3$  groups are introduced for each Sn atom. Unlike C, atomic fractions of oxygen present in the material are not introduced during deposition, but are the results of post-deposition oxidation and indicative of a chemically unstable material. In our previous work, on a/nc-Ge:H, a relation was established between i) processing conditions, ii) material density/porosity and iii) the occurrence and degree of post-deposition oxidation [24–26,40].

The relatively high carbon integration, in reference to that of Sn, introduces certain challenges to the processing of a chemically stable, low-bandgap energy, intrinsic ( $E_{\text{act}} \approx 0.5E_{04}$ ) Ge:H alloy.  $E_{04}$  generally increases with increasing  $at_{\text{C}}$ , as can be observed in Fig. 4I–II, especially in reference to the densest Ge:H films which have an  $E_{04}$  of  $\approx 1.1\text{eV}$ . This is also owing to the increase of  $at_{\text{O}}$  in the films, which scales with the  $at_{\text{C}}$ , as can be observed in Fig. 4IV. This relation is not unexpected, as C-integration is predominantly expected to occur through the integration of  $\text{CH}_n$  groups from the TMT precursors. The integration of  $\text{CH}_n$  groups results in an increase of material porosity, which is reflected by the change in  $n_{@600\text{nm}}$  in Fig. 4II, as a function of  $at_{\text{C}}$ . This relation between  $\text{CH}_n$  flux and porosity is in line with observations from the PECVD and glow-discharge CVD processing of SiC:H using a  $\text{CH}_4$  precursor, where it was concluded that more  $\text{CH}_n$  than atomic C was build into the material [41], resulting in a deposition rate increase [42] and increase of the H-concentration [43] with increasing  $\text{CH}_4$  flow rate in reference to  $\text{SiH}_4$ . As a consequence, the mechanisms responsible for the increase in  $at_{\text{C}}$  will also result in an increase of material porosity, and consequently influence the oxidation behaviour [24–26,40].

Notably,  $E_{04}$  is not increased for all samples, despite a decrease of  $n_{@600\text{nm}}$ . If we consider the samples with  $E_{04} \leq 1.1\text{eV}$ , it can be observed that they all have a relatively high Sn concentration in

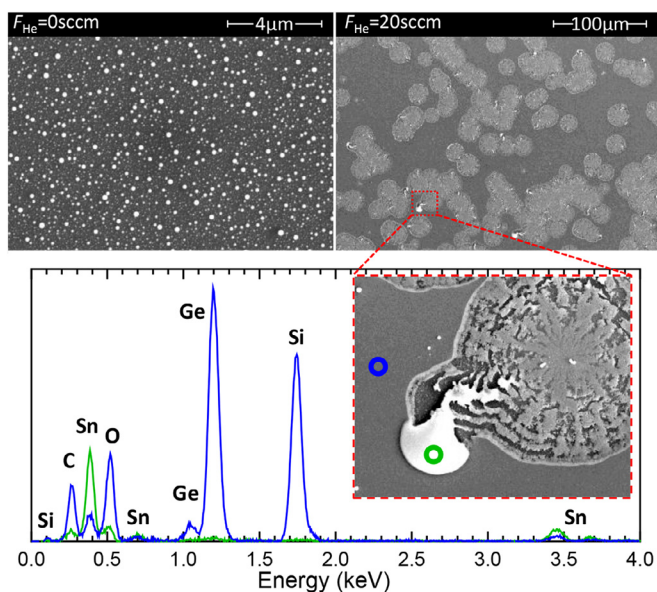


**Fig. 3.** SEM (top) and EDX (bottom) measurements of the surface of a-GeSn:H samples with  $\delta=100$ . SEM images are shown of samples with  $F_{\text{He}}=0\text{sccm}$  (top-left) and  $F_{\text{He}}=20\text{sccm}$  (top-right). EDX measurements shown after background subtraction of a position on a Sn cluster (green) and on the amorphous GeSn:H phase (blue), as indicated in the inset. Identification of the various peaks indicated in plot. (For interpretation of the references to colour in this figure legend, the reader is referred to the web version of this article.)

reference to carbon concentration, as indicated by the  $at_{\text{Sn}}/at_{\text{C}}$  in Fig. 4III. This indicates that through Sn-integration relatively low  $E_{04}$  values can be realized despite the presence of carbon.

The carbon integration does not exclusively have negative effects on the film properties however. Using GeSnC:H in p-i-n or n-i-p junctions, for instance for PV applications, requires the alloy to be (close to) intrinsic. In intrinsic materials the concentration of electrons and holes are roughly equal, with the Fermi level positioned halfway the bandgap, so with  $E_{\text{act}} \approx 0.5E_{\text{G}}$ . Earlier work resulted in the belief that the a/nc-Ge:H phase has a relatively high defect density, with an n-type nature, and  $E_{\text{act}} \ll 0.5E_{\text{G}}$ . This is likely related to the behaviour of hydrogen in germanium, as hydrogen does not readily passivate germanium dangling bonds [24–26]. The poor hydrogen passivating behaviour can also be observed by considering the icon colour in Fig. 4IV, which shows that the number of hydrogen atoms bonded to C in reference to Ge is in the range of 60–80% at only an  $at_{\text{C}}=2\text{--}8\%$ .

It can be observed in Fig. 4I that the  $E_{\text{act}}$  significantly increases with increasing  $at_{\text{C}}$ . Qualitatively, the increases of  $E_{\text{act}}$  with  $at_{\text{C}}$  can be expected, as for an intrinsic material  $E_{\text{act}} \approx 0.5E_{04}$ . Notably

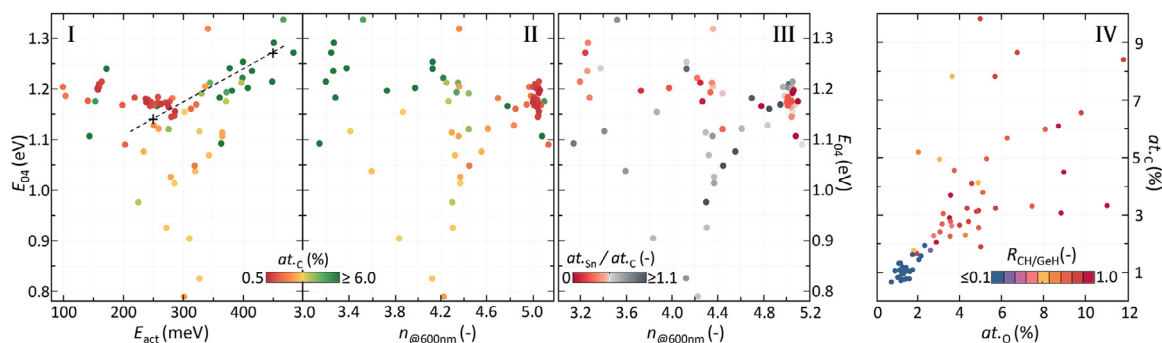


**Fig. 4.** The influence of carbon on the opto-electrical properties of GeSn:H. I and II show  $E_{04}$  as a function of  $E_{\text{act}}$  and  $n_{@600\text{nm}}$ , respectively, with colour indicating  $at_{\text{C}}$ . In III  $E_{04}$  is plotted as a function of  $n_{@600\text{nm}}$ , with colour indicating in  $at_{\text{Sn}}/at_{\text{C}}$ . In IV  $at_{\text{C}}$  is plotted as a function of  $at_{\text{O}}$ , with colour indicating in  $R_{\text{CH}/\text{GeH}}$ .

**Table 1**

Deposition conditions of amorphous and nano-crystalline GeSn:H samples; radiofrequency power ( $P_{\text{RF}}$ ), pressure ( $p$ ), substrate temperature ( $T_{\text{S}}$ ), germane flow rate ( $F_{\text{GeH}_4}$ ) and  $\text{H}_2$  flow rate ( $F_{\text{H}_2}$ ). The TMT duty cycle ( $\delta$ ) is varied between 429 and 12000.

|         | $P_{\text{RF}}$<br>(mW.cm <sup>-2</sup> ) | $p$<br>(mbar) | $T_{\text{S}}$<br>(°C) | $F_{\text{GeH}_4}$<br>(sccm) | $F_{\text{H}_2}$<br>(sccm) |
|---------|---|---------------|------------------------|------------------------------|----------------------------|
| a-Ge:H  | 14.9                                      | 4             | 210–290                | 2                            | 200                        |
| nc-Ge:H | 24.8                                      | 1             | 210–290                | 1                            | 200                        |

however, the increase in  $E_{\text{act}}$  exceeds that of  $E_{04}$ . Considering the trendline added to Fig. 4I, an  $E_{04}$  increase of 150meV results in an 200meV increase of  $E_{\text{act}}$ . Based on Fig. 4I we therefore speculate that carbon, or the  $\text{CH}_n$  groups dissociated from the TMT precursor, effectively passivate the Ge-dangling bonds and decrease the defect density in reference to an unalloyed a/nc-Ge:H phase. This defect passivating behaviour was previously demonstrated for oxygen, as a decrease of  $\sigma_{\text{d}}$  despite a decrease in  $E_{\text{act}}$  was observed in a/nc-Ge:H films upon post-deposition oxidation [24]. It should be noted that this increase of  $E_{\text{act}}$  in Fig. 4I occurs despite the fact that  $at_{\text{O}}$  scales with  $at_{\text{C}}$  (Fig. 4IV) and that oxygen integration generally results in a strong decrease of  $E_{\text{act}}$ , as the  $\text{GeO}_x$  phase has a strong n-type nature [24,25]. This demonstrates that the Ge-C bond has an energetic nature that is either p-type or close to intrinsic.

Next we consider the effect of  $\delta$  in some more detail, as presented in Fig. 5. For the two amorphous series (red and black icons) the observed trends as a function of  $\delta$  match, while the trends for the series processed under nano-crystalline conditions (blue icons) is dissimilar for most measured metrics. For the series processed under amorphous conditions, the carbisation of the films appears to have a dominant influence on their respective opto-electrical properties. With increasing  $\delta$ ,  $at_{\text{C}}$  decreases, resulting in an increase of  $n_{@600\text{nm}}$  and decrease of  $at_{\text{O}}$  and  $E_{04}$ . As discussed before,  $E_{\text{act}}$  scales with  $at_{\text{C}}$ , while  $\sigma_{\text{d}}$  decreases with increasing  $E_{\text{act}}$ , as was observed before in Ge:H films [24,25]. As a consequence the highest photoresponses ( $\sigma_{\text{ph}}/\sigma_{\text{d}}$ ) are achieved at relatively low  $\delta$ , so high  $at_{\text{C}}$  values.

The opto-electrical properties of the samples processed under nano-crystalline conditions show some deviating behaviour. Fig. 5 (blue icons) shows that exclusively for the nano-crystalline samples a decrease of  $\delta$  results in a decrease of  $E_{04}$ , an increase of  $E_{\text{act}}$  and decrease of  $\sigma_{\text{d}}$ . These samples have a relatively low  $at_{\text{O}}$  and  $at_{\text{C}}$ , and a significantly higher  $at_{\text{Sn}}/at_{\text{C}}$  than the amorphous samples.

In Fig. 6 the  $at_{\text{Sn}}$  of all samples in which a crystalline peak was observed is presented as a function of the exact Raman shift of the crystalline Ge peak as well as the crystalline phase fraction. The figure not only shows that the  $at_{\text{Sn}}$  increases with the  $\chi_{\text{C}}$ , it also shows that the c-Ge peak position is shifted downward

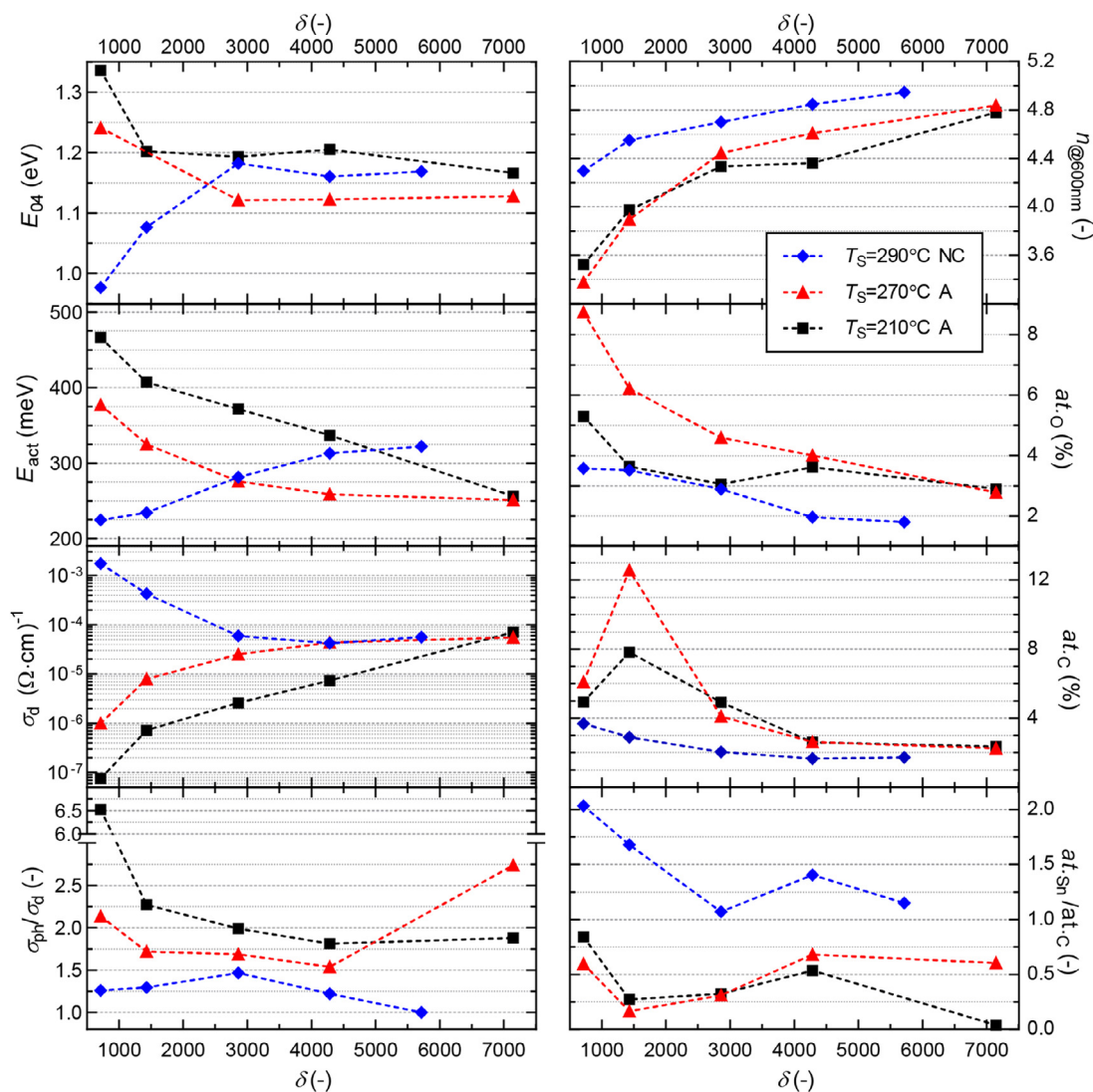


**Fig. 5.** Influence of duty cycle on the elemental composition and opto-electrical properties of 4 different series of GeSn:H samples. All samples are processed at  $F_{He}=5\text{scm}$  and amorphous conditions, with the exception of samples processed at  $T_S=290^\circ\text{C}$  (blue), which are processed at nano-crystalline conditions (as indicated in Table 1). For all series the close time was varied at a fixed open time of 7ms. (For interpretation of the references to colour in this figure legend, the reader is referred to the web version of this article.)

with increasing  $at_{Sn}$  and  $\chi_C$ . This observation is in line with earlier reports, where a decrease of the Raman-shift of the c-Ge peak was observed in epitaxially grown crystalline GeSn with increasing  $at_{Sn}$  [5,15,17,18]. The relation between the  $\chi_C$ ,  $at_{Sn}$  and c-Ge peak position suggest that the crystalline phase in the heterogeneous nc-GeSn:H material is in fact a GeSn crystalline phase. Additionally, the relation between  $\chi_C$ ,  $at_{Sn}/at_C$  and  $at_{Sn}$  suggests a growth mechanism in which Sn is favourably integrated in the crystalline phase in reference to the amorphous phase.

Moreover, if we consider the relation between the  $at_{Sn}$  and the Raman-shift of the crystalline GeSn peak reported in other works, as indicated by the coloured lines and areas in Fig. 6, and compare it to the relation observed in our experimental data, it can be concluded the Sn concentration is likely much higher in the crystalline phase than in the amorphous phase. Extrapolating the data presented in Fig. 6, an  $at_{Sn}$  of 15.5–17.5% could be expected for the nc-GeSn:H sample with an  $288.7\text{cm}^{-1}$  c-Ge peak position. Considering the  $\chi_C$  of around 50% and the overall  $at_{Sn}$  of 7.8%, the amorphous phase is expected to have a very low  $at_{Sn}$  of 0–1.8%. This means that the nc-GeSnC:H samples have a strongly heterogeneous

nature, consisting of GeSn crystals embedded in an predominantly amorphous germanium-carbide phase. Considering the relation between  $at_{Sn}$  and  $E_G$  presented in [21,44], the GeSn crystals can be expected to have an  $E_G$  in the range of 0.5–0.55eV.

In determining the optimal processing regimes, it can be established that the lowest  $E_{04}$  are achieved for the nc-GeSn:H samples at low  $\delta$  of  $\approx <2000$ . For moderate duty cycles, the a-GeSn:H samples processed at elevated temperature exhibit lower  $E_{04}$  values, as well as lower  $\sigma_d$  and higher  $\sigma_d/\sigma_{ph}$  values. While both these series are processed at elevated temperature, the difference between these series is mainly the  $P_{RF}$  at which they are processed. In the next section we will therefore look at the effect of these two processing conditions in more detail.

### 3.0.2. Temperature

First we consider the influence of  $T_S$  on three sets of samples, with different  $F_{He}$  and  $\delta$ . Two main observations can be made from Fig. 7. Firstly, independent of the TMT dilution in  $F_{He}$ , processing stable, dense amorphous GeSn films with high  $n_{@600nm}$  and low

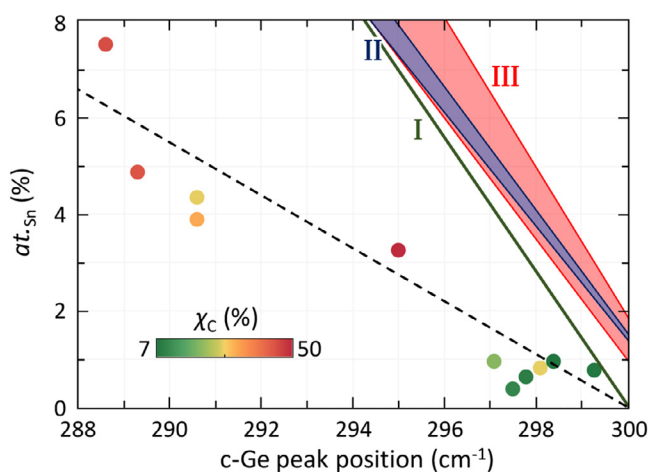


**Fig. 6.**  $at_{Sn}$  as a function of the measured Raman shift of the c-Ge peak of all samples with  $\chi_c$ . Colour indicates the  $\chi_c$  of the samples. A trend-line (black, dashed) is added for the samples measured in this work. Additional lines and areas are present in the graph, indicating the relation between  $at_{Sn}$  and the Raman shift of the c-Ge peak for epitaxially grown c-GeSn films according to I (green) [18], II (blue) [28] and III (red) [17]. (For interpretation of the references to colour in this figure legend, the reader is referred to the web version of this article.)

$E_{04}$  is very challenging for low  $\delta$ -values. Even at elevated  $T_S$ , which generally results in dense material growth for Ge:H and SiGe:H films [25], porous material growth cannot be avoided as indicated by the low  $n_{@600nm}$ -values. The highest  $n_{@600nm}$  of the two series with  $\delta=429$ , in reference to the series processed at  $\delta=3333$ , is 1.5 lower. As a consequence the samples readily oxidize, as indicated by the high  $at_{O_0}$ . This oxidation behaviour makes the processing of chemically stable amorphous a-GeSn:H at relatively low  $\delta$  not feasible.

The second observation is related to the electrical behaviour of the three series of samples. Considering the influence of  $T_S$  on the  $\delta=3333$  samples, it can be observed that with increasing  $T_S$ ,  $n_{@600nm}$  increases, further reducing oxidation and increasing  $E_{04}$ .  $at_C$  and  $at_{Sn}/at_C$  seem to remain relatively unchanged as a function of  $T_S$ . With the decrease of  $at_{O_0}$ ,  $E_{act}$  is observed to increase and  $\sigma_{ph}/\sigma_d$  to decrease. This is in line with our earlier reports on the oxidation behaviour of hydrogenated germanium, where it was observed that oxygen in germanium passivates defects, decreasing the defect density, but creating Ge-O<sub>x</sub> bonds with an n-type nature that decrease  $E_{act}$  [24].

The difference in electrical behaviour between the low- $\delta$  and  $\delta=3333$  samples seems to suggest that carbon, or potentially Sn, in addition to oxygen has the ability to passivate the Ge-defects. This can be concluded from the change in  $E_{act}$  in reference to the change in  $E_{04}$ . For an undoped material a change of  $\Delta E_{act}=0.5\Delta E_{04}$  can be expected. However, it can be observed in Fig. 7 that the 200-300meV  $E_{act}$  difference between the low- $\delta$  and  $\delta=3333$  samples far exceeds the 100-150meV  $E_{04}$  difference, so  $\Delta E_{act} \gg 0.5\Delta E_{04}$ , which is similar to the observation indicated by the trendline in Fig. 4I-II. As a result of the much higher  $E_{act}$ ,  $\sigma_d$  is 5-3 orders of magnitude lower for the low- $\delta$  samples in reference to the  $\delta=3333$  samples and the  $\sigma_{ph}/\sigma_d$  is generally higher for the samples with high  $at_C$ . This indicates that without the presence of some element to passivate the germanium defects, other than hydrogen which is not very effective at doing so, it is challenging to achieve favourable electrical material characteristics.

### 3.0.3. Power

Next we consider the influence of power. Fig. 8 shows that with increasing power,  $E_{04}$  continuously increases. While this increase

can be ascribed to an increasing  $at_{O_0}$  in the 6-10W range, the origin of this increase in the 2-6W range is unclear. With increasing  $P_{RF}$ , more energy is supplied to the plasma, more effectively dissociating the precursor gasses and resulting in a larger overall growth flux. As a consequence, the growth rate is continually increased from about 10nm/min at 3W to 21nm/min at 10W. More porous growth, that is more susceptible to oxidation, could be expected as a result of this growth-rate increase. While this could account for the increase of  $at_{O_0}$  and  $E_{04}$  for  $P_{RF} \geq 8W$ , a similar porosification and decrease of  $n_{@600nm}$  are not observed at lower powers.

In addition to an overall growth flux increase, a change in  $P_{RF}$  can also change the growth flux composition. Stronger bonds require more energy for dissociation. At higher  $P_{RF}$ , more energy is supplied to the plasma. As a consequence, in relative terms, the dissociation of stronger bonds is increased at higher power in reference to the dissociation of weaker bonds. The fraction of compounds with high dissociation energy precursors in the growth flux composition will therefore increase with increasing  $P_{RF}$ .

Of the precursors introduced during deposition of GeSn:H, dissociation of a methyl group from the TMT precursors only requires 227 kJ/mol [45]. However, further dissociating the methyl group itself requires a relatively large amount of energy, as the dissociation of a single hydrogen atom from CH<sub>3</sub> requires 457kJ/mol and dissociating a second hydrogen atom requires an additional 418 kJ/mol [46], which is similar to that of H<sub>2</sub> at 436kJ/mol. The dissociation of GeH<sub>4</sub>, on the other hand, only requires about 350kJ/mol [47,48].

This means that with increasing  $P_{RF}$ , in relative terms, the dissociation of H<sub>2</sub> and CH<sub>2-3</sub> will increase in reference to GeH<sub>4</sub> dissociation, which in turn will increase in reference to dissociation of CH<sub>3</sub> from Sn.

The consequence of these growth-flux-composition effects as a function of  $P_{RF}$  can be observed in the vibrational spectroscopy and EDX spectroscopy measurements performed on the films. As shown in Fig. 8,  $at_{Sn}$  continuously decreases with increasing  $P_{RF}$  as the relative fraction of Sn(CH<sub>n</sub>)<sub>n</sub> radicals in the growth flux is decreased.

Additionally, two effects occur: I. the dissociation of the neutral GeH<sub>4</sub> precursor to GeH<sub>1-3</sub> neutral radicals and ions is increased in reference to the dissociation of CH<sub>3</sub> groups from TMT and II. in reference to GeH<sub>4</sub> dissociation, CH<sub>3</sub> dissociation is increased with increasing  $P_{RF}$  and the fraction of smaller CH<sub>1-2</sub> radicals in the growth flux is increased. As a consequence, the ratio of the C-H bonds in reference to the Ge-H bonds observed in the infrared spectra generally decreases with increasing  $P_{RF}$ , as indicated by  $R_{CH/GeH}$ , and the fraction of amorphous C-C vibrations continuously increases, as indicated by  $R_{aC/aGe}$ . It should be noted that the increase of atomic hydrogen etching in reference to material growth, resulting from more effective CH<sub>n</sub> and H<sub>2</sub> dissociation, could also play a role in the increase of  $R_{aC/aGe}$  with  $P_{RF}$ .

The opto-electrical film properties, then, are a result of the material phase fraction, void fraction, hydrogenation and the level of tin and carbon integration. To achieve favourable film properties, sufficient control has to be exerted over the film growth. From the preceding results we can conclude that the growth flux composition can be controlled to some extent through the  $P_{RF}$ . With increasing  $P_{RF}$  the dissociation of methyl groups, and to a lesser extent germane, in reference to TMT is increased. This control is complicated however by an overall increase of the growth flux and consequently more porous growth, with increasing  $P_{RF}$ . The deposition temperature is a possible processing condition for controlling the void fraction. Material densification occurs with increasing  $T_S$ . Care has to be taken however considering the solubility of Sn. The void fraction can also be influenced through the duty cycle and potentially through the dilution of GeH<sub>4</sub> in H<sub>2</sub>, as atomic hy-

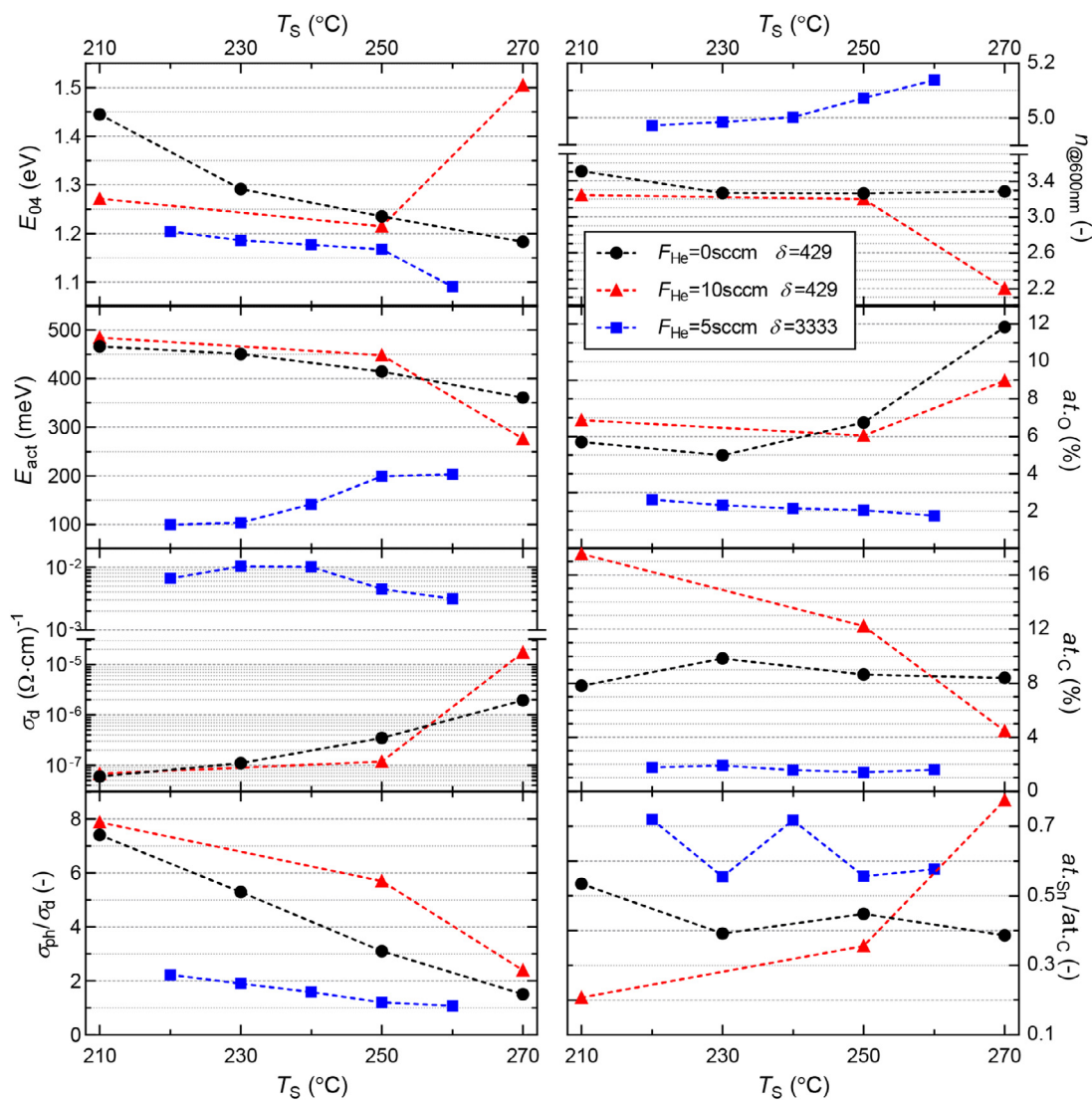


**Fig. 7.** Influence of deposition temperature on the elemental composition and opto-electrical properties of 3 different series of GeSn:H samples. All samples are processed at amorphous conditions (as indicated in Table 1).

drogen etching in reference to the growth flux is increased with increasing hydrogen dilution. Additionally, similar to the duty cycle, the  $F_{\text{GeH}_4}/F_{\text{H}_2}$  ratio upsets the balance between  $\text{CH}_n$ ,  $\text{Sn}(\text{CH}_n)_n$  and  $\text{GeH}_n$  in the growth flux. The experimental results of a series of samples for which  $F_{\text{GeH}_4}/F_{\text{H}_2}$  is varied is available in the supplementary information.

#### 4. Conclusion

In this work, the first steps towards the PECVD processing of a chemically stable, low- $E_G$  and intrinsic GeSn:H alloy are presented. The processing of such an alloy, using a TMT precursor, is a complicated process with a number of inherent challenges.

Among these is the relatively low melting point of Sn, resulting in the formation of Sn-clusters at high TMT injection levels. The Sn-clustering prevents the formation of a low- $E_G$  GeSn:H phase and introduces a limit to the amount of TMT that can be injected into the plasma. An additional challenge is the TMT precursor itself, through which four  $\text{CH}_3$  groups are introduced into the reactor for each Sn-atom. We demonstrate in this work that manag-

ing the carbon integration into the material is crucial for obtaining low- $E_G$  and chemically stable materials.

As a result of large  $\text{CH}_n$  fluxes, the porosity is generally observed to increase with the carbon concentration, resulting in increased oxidation of the samples. Surprisingly however, some C-integration seems favourable from a defect engineering perspective. Strong increases of  $E_{\text{act}}$ , far exceeding the increase in  $E_G$ , has been observed in amorphous GeSnC:H films with  $\text{at.}_{\text{Sn}}$  as lows as 3–6%. This suggest that C effectively passivates the dominant defect type in Ge:H, resulting in films with a Fermi level closer to that of an intrinsic material. Additionally, C readily reacts with H, with the fraction of C-H bonds far exceeding the fraction of Ge-H bonds already at carbon concentration of a few percent.

Considering the optical behaviour of the films, low  $E_{04}$  are only realized at relatively high Sn/C ratios. High Sn to C ratios are predominantly realized for samples with a relatively high crystallinity. In fact, we show that low duty cycles, so high levels of Sn and C integration, are only feasible for highly crystalline materials. nc-GeSn(C):H films with  $\chi_{\text{C}}=50\%$  are processed with a highly heterogeneous nature, consisting of GeSn crystals with 15.5–17.5% Sn embedded in an a-GeC:H phase in which almost no Sn is present. Such heterogeneous nc-GeSnC:H films could provide a potential

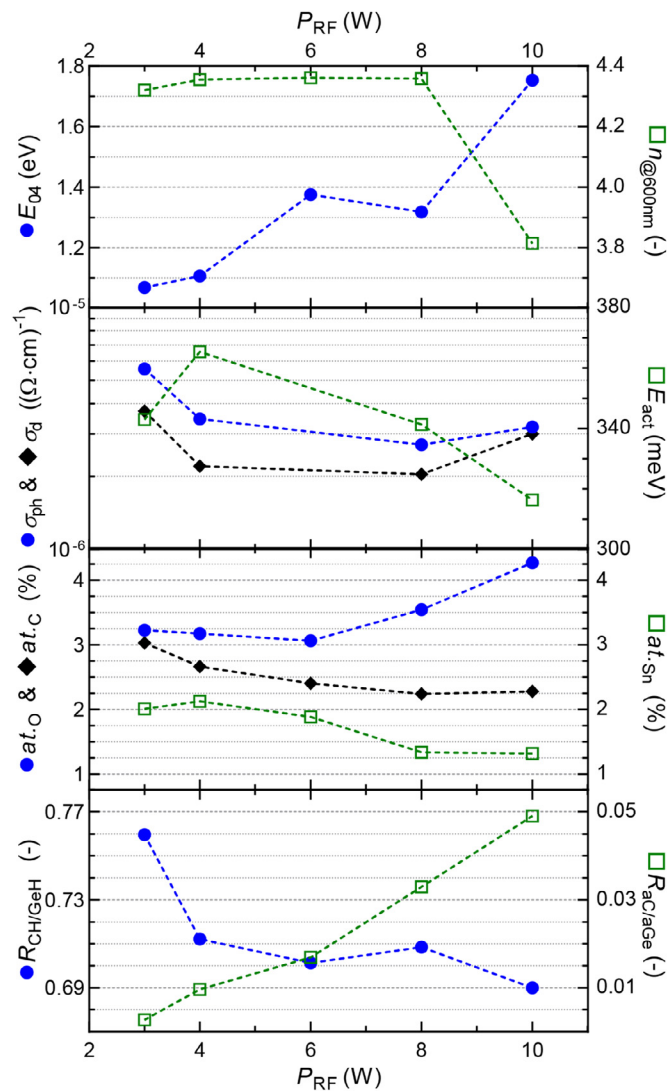


**Fig. 8.** Influence of RF power on the elemental composition and opto-electrical properties of GeSn:H samples. Samples processed at amorphous conditions, with  $T_s=230$  °C,  $F_{He}=5$  sccm and  $\delta=2857$ . The metrics represented by the different icon types are indicated on the respective vertical axes.

route towards a low bandgap energy group IV alternative for photovoltaic multijunction applications.

#### Data availability

The data that supports the findings of this study are available within the article.

#### Declaration of Competing Interest

The authors declare that they have no known competing financial interests or personal relationships that could have appeared to influence the work reported in this paper.

#### CRediT authorship contribution statement

**Thierry de Vrijer:** Conceptualization, Formal analysis, Investigation, Writing – original draft, Writing – review & editing, Visualization, Supervision. **Koos Roodenburg:** Investigation. **Federica Saitta:** Investigation. **Thijs Blackstone:** Investigation. **Gianluca Limodio:** Investigation. **Arno H.M. Smets:** Conceptualization, Writing – review & editing, Supervision, Funding acquisition.

#### Acknowledgments

The authors would like to gratefully acknowledge the financial support from the Netherlands Organization for Scientific Research (NWO) Solar to Products grant awarded to Arno Smets and the support provided by Shell International Exploration & Production New Energies Research & Technology Dense Energy Carriers Program.

#### Supplementary material

Supplementary material associated with this article can be found, in the online version, at [10.1016/j.apmt.2022.101450](https://doi.org/10.1016/j.apmt.2022.101450)

#### References

- [1] R. Soref, Mid-infrared photonics in silicon and germanium, *Nat. Photon.* 4 (8) (2010) 495–497, doi:[10.1038/nphoton.2010.171](https://doi.org/10.1038/nphoton.2010.171).
- [2] S. Wirths, D. Buca, S. Mantl, Si-ge-sn alloys: from growth to applications, *Prog. Cryst. Growth Charact. Mater.* 62 (1) (2016) 1–39, doi:[10.1016/j.pcrysgrow.2015.11.001](https://doi.org/10.1016/j.pcrysgrow.2015.11.001).
- [3] Y. Zhou, W. Dou, W. Du, T. Pham, S.A. Ghetmiri, S. Al-Kabi, A. Mosleh, M. Alher, J. Margetis, J. Tolle, G. Sun, R. Soref, B. Li, M. Mortazavi, H. Naseem, S.Q. Yu, Systematic study of gesn heterostructure-based light-emitting diodes towards mid-infrared applications, *J. Appl. Phys.* 120 (2) (2016) 023102, doi:[10.1063/1.4958337](https://doi.org/10.1063/1.4958337).
- [4] C.L. Senaratne, P.M. Wallace, J.D. Gallagher, P.E. Sims, J. Kouvetakis, J. Menéndez, Direct gap  $ge_{1-x}sn_x$  alloys: fabrication and design of mid-IR photodiodes, *J. Appl. Phys.* 120 (2) (2016) 025701, doi:[10.1063/1.4956439](https://doi.org/10.1063/1.4956439).
- [5] P. Pearce, T. Wilson, A. Johnson, N. Ekins-Daukes, Characterization of Signs for Use as a 1 Ev Sub-cell in Multi-junction Solar Cells, in: 2018 IEEE 7th World Conference on Photovoltaic Energy Conversion (WCPEC) (A Joint Conference of 45th IEEE PVSEC, 28th PVSEC & 34th EU PVSEC), IEEE, 2018, pp. 0943–0948, doi:[10.1109/PVSEC.2018.8547764](https://doi.org/10.1109/PVSEC.2018.8547764).
- [6] R. Roucka, A. Clark, B. Landini, Si-ge-sn Alloys with 1.0 Ev Gap for CPV Multijunction Solar Cells, in: AIP Conference Proceedings, Vol. 1679, 2015, p. 040008, doi:[10.1063/1.4931519](https://doi.org/10.1063/1.4931519).
- [7] S. Assali, J. Nicolas, O. Moutanabbir, Enhanced sn incorporation in gesn epitaxial semiconductors via strain relaxation, *J. Appl. Phys.* 125 (2) (2019) 025304, doi:[10.1063/1.5050273](https://doi.org/10.1063/1.5050273).
- [8] S. Su, W. Wang, B. Cheng, W. Hu, G. Zhang, C. Xue, Y. Zuo, Q. Wang, The contributions of composition and strain to the phonon shift in alloys, *Solid State Commun.* 151 (8) (2011) 647–650, doi:[10.1016/j.ssc.2011.01.017](https://doi.org/10.1016/j.ssc.2011.01.017).
- [9] M. Oehme, K. Kosteci, M. Schmid, F. Oliveira, E. Kasper, J. Schulze, Epitaxial growth of strained and unstrained gesn alloys up to 25% sn, *Thin Solid Films* 557 (2014) 169–172, doi:[10.1016/j.tsf.2013.10.064](https://doi.org/10.1016/j.tsf.2013.10.064).
- [10] W. Wang, L. Li, Q. Zhou, J. Pan, Z. Zhang, E.S. Tok, Y.C. Yeo, Tin surface segregation, desorption, and island formation during post-growth annealing of strained epitaxial  $ge_{1-x}sn_x$  layer on  $ge(001)$  substrate, *Appl. Surf. Sci.* 321 (2014) 240–244, doi:[10.1016/j.apsusc.2014.10.011](https://doi.org/10.1016/j.apsusc.2014.10.011).
- [11] R. Hickey, N. Fernando, S. Zollner, J. Hart, R. Hazbun, J. Kolodzey, Properties of pseudomorphic and relaxed germanium $_{1-x}$ tin $_x$  alloys ( $x < 0.185$ ) grown by MBE, *J. Vacuum Sci. Technol. B, Nanotechnol. Microelectron.* 35 (2) (2017) 021205, doi:[10.1116/1.4975149](https://doi.org/10.1116/1.4975149).
- [12] J. Bennett, R. Egerton, Fabrication of  $sn_xge_{1-x}$  thin films with non-equilibrium composition, *Vacuum* 47 (12) (1996) 1419–1422, doi:[10.1016/S0042-207X\(96\)00219-9](https://doi.org/10.1016/S0042-207X(96)00219-9).
- [13] J. Zheng, Z. Liu, Y. Zhang, Y. Zuo, C. Li, C. Xue, B. Cheng, Q. Wang, Growth of high-sn content (28%) gesn alloy films by sputtering epitaxy, *J. Cryst. Growth* 492 (2018) 29–34, doi:[10.1016/j.jcrysgro.2018.04.008](https://doi.org/10.1016/j.jcrysgro.2018.04.008).
- [14] L. Zhang, Y. Wang, N. Chen, G. Lin, C. Li, W. Huang, S. Chen, J. Xu, J. Wang, Raman scattering study of amorphous gesn films and their crystallization on si substrates, *J. Non Cryst. Solids* 448 (2016) 74–78, doi:[10.1016/j.jnoncrysol.2016.07.007](https://doi.org/10.1016/j.jnoncrysol.2016.07.007).
- [15] J. Margetis, A. Mosleh, S.A. Ghetmiri, S. Al-Kabi, W. Dou, W. Du, N. Bhargava, S.-Q. Yu, H. Profijt, D. Kohen, R. Loo, A. Vohra, J. Tolle, Fundamentals of  $ge_{1-x}sn_x$  and  $si_yge_{1-x-y}sn_x$  RPCVD epitaxy, *Mater. Sci. Semicond. Process.* 70 (2017) 38–43, doi:[10.1016/j.mssp.2016.12.024](https://doi.org/10.1016/j.mssp.2016.12.024).
- [16] J. Aubin, J. Hartmann, A. Gassenq, L. Milord, N. Pauc, V. Reboud, V. Calvo, Impact of thickness on the structural properties of high tin content gesn layers, *J. Cryst. Growth* 473 (2017) 20–27, doi:[10.1016/j.jcrysgro.2017.05.006](https://doi.org/10.1016/j.jcrysgro.2017.05.006).
- [17] N. von den Driesch, D. Stange, S. Wirths, G. Mussler, B. Hölländer, Z. Ikonik, J.M. Hartmann, T. Stoica, S. Mantl, D. Grützmacher, D. Buca, Direct bandgap group IV epitaxy on si for laser applications, *Chem. Mater.* 27 (13) (2015) 4693–4702, doi:[10.1021/acs.chemmater.5b01327](https://doi.org/10.1021/acs.chemmater.5b01327).
- [18] V.R. D'Costa, Y. Fang, J. Mathews, R. Roucka, J. Tolle, J. Menéndez, J. Kouvetakis, Sn-alloying as a means of increasing the optical absorption of ge at the c- and l-telecommunication bands, *Semicond. Sci. Technol.* 24 (11) (2009) 115006, doi:[10.1088/0268-1242/24/11/115006](https://doi.org/10.1088/0268-1242/24/11/115006).
- [19] M. Bauer, J. Taraci, J. Tolle, A.V.G. Chizmeshya, S. Zollner, D.J. Smith, J. Menéndez, C. Hu, J. Kouvetakis, Ge-sn semiconductors for band-gap and lattice engineering, *Appl. Phys. Lett.* 81 (16) (2002) 2992–2994, doi:[10.1063/1.1515133](https://doi.org/10.1063/1.1515133).

- [20] R. Temkin, G. Connell, W. Paul, Structural and optical properties of amorphous  $Ge_xSn_{1-x}$  alloys, *Solid State Commun.* 11 (1972) 1591–1595.
- [21] I. Chambouleyron, F.C. Marques, Use of hydrogenation in the study of the properties of amorphous germanium tin alloys, *J. Appl. Phys.* 65 (4) (1989) 1591–1597, doi:10.1063/1.342950.
- [22] I. Chambouleyron, F.C. Marques, J.P. de Souza, I.J.R. Baumvol, Structure and composition of amorphous  $Ge_{1-x}Sn_x$  thin films, *J. Appl. Phys.* 63 (11) (1988) 5596–5598, doi:10.1063/1.340338.
- [23] S. Sato, N. Yamaguchi, H. Ozaki, Pseudogap of energy in amorphous ge-sn films, *J. Phys. Soc. Jpn.* 33 (5) (1972) 1497, doi:10.1143/JPSJ.33.1497.
- [24] T. de Vrijer, A. Ravichandran, B. Bouazzata, A.H. Smets, The impact of processing conditions and post-deposition oxidation on the opto-electrical properties of hydrogenated amorphous and nano-crystalline germanium films, *J. Non Cryst. Solids* 553 (2021) 120507, doi:10.1016/j.jnoncrysol.2020.120507.
- [25] T. de Vrijer, J.E. van Dingen, P.J. Roelandschap, K. Roodenburg, A.H. Smets, Improved PECVD processed hydrogenated germanium films through temperature induced densification, *Mater. Sci. Semicond. Process.* 138 (2022) 106285, doi:10.1016/j.mssp.2021.106285.
- [26] T. de Vrijer, B. Bouazzata, A. Ravichandran, J. van Dingen, P. Roelandschap, K. Roodenburg, S. Roerink, F. Saitta, T. Blackstone, A. Smets, Opto-electrical properties of group IV alloys : the inherent challenges of processing hydrogenated germanium, *Adv. Sci.* (2022).
- [27] K. Yoshioka, R. Yokogawa, A. Ogura, Anisotropic biaxial stress evaluation in metal-organic chemical vapor deposition grown  $Ge_{1-x}Sn_x$  mesa structure by oil-immersion raman spectroscopy, *Thin Solid Films* 697 (2020) 137797, doi:10.1016/j.tsf.2020.137797.
- [28] K. Suda, N. Sawamoto, H. Machida, M. Ishikawa, H. Sudoh, Y. Ohshita, I. Hirose, A. Ogura, Role of  $H_2$  supply for Sn incorporations in MOCVD  $Ge_{1-x}Sn_x$  epitaxial growth, *J. Cryst. Growth* 468 (2017) 605–609, doi:10.1016/j.jcrysgro.2016.12.085.
- [29] C. Zoita, C. Grigorescu, I. Vasiliu, I. Feraru, Influence of process parameters on structure and optical properties of gec thin films deposited by RF magnetron sputtering, *Thin Solid Films* 519 (12) (2011) 4101–4104, doi:10.1016/j.tsf.2011.01.204.
- [30] N. Saito, I. Nakaaki, T. Yamaguchi, S. Yoshioka, S. Nakamura, Influence of deposition conditions on the properties of a-gec:h and a-ge:h films prepared by r.f. magnetron sputtering, *Thin Solid Films* 269 (1–2) (1995) 69–74, doi:10.1016/0040-6090(95)06671-3.
- [31] M. Wojdyr, Fityk : a general-purpose peak fitting program, *J. Appl. Crystallogr.* 43 (5) (2010) 1126–1128, doi:10.1107/S0021889810030499.
- [32] T. de Vrijer, B. Bouazzata, A.H.M. Smets, Spectroscopic review of hydrogenated, carbonated and oxygenated group IV alloys, *Vibrat. Spectrosc.* (2022).
- [33] A.H.M. Smets, M.C.M. van de Sanden, Relation of the si-h stretching frequency to the nanostructural si-h bulk environment, *Phys. Rev. B* 76 (7) (2007) 073202, doi:10.1103/PhysRevB.76.073202.
- [34] M. Cardona, Vibrational spectra of hydrogen in silicon and germanium, *Physica Status Solidi (B)* 118 (2) (1983) 463–481, doi:10.1002/pssb.2221180202.
- [35] M.S. Abo-Ghazala, S.A. Hazmy, Hydrogen bonding in hydrogenated amorphous germanium, *Tsinghua Sci. Technol.* 9 (2) (2004) 177–180.
- [36] M. Künle, T. Kaltenbach, P. Löper, A. Hartel, S. Janz, O. Eibl, K.G. Nickel, Si-rich a-sic:h thin films: structural and optical transformations during thermal annealing, *Thin Solid Films* 519 (1) (2010) 151–157, doi:10.1016/j.tsf.2010.07.085.
- [37] A. Oliveira, M. Carreño, Post thermal annealing crystallization and reactive ion etching of sic films produced by PECVD, *J. Non Cryst. Solids* 352 (9–20) (2006) 1392–1397, doi:10.1016/j.jnoncrysol.2006.01.075.
- [38] S. Ray, D. Das, A. Barua, Infrared vibrational spectra of hydrogenated amorphous silicon carbide thin films prepared by glow discharge, *Solar Energy Mater.* 15 (1987) 45–57.
- [39] A. Morimoto, T. Miura, M. Kumeda, T. Shimizu, Glow discharge a-si<sub>1-x</sub>C<sub>x</sub>: h films studied by ESR and IR measurements, *Jpn. J. Appl. Phys.* 21 (1982) (Part 2, No. 2) L119–L121, doi:10.1143/JJAP.21.L119.
- [40] T. de Vrijer, A.H.M. Smets, Infrared analysis of artificial (photo)synthesis in hydrogenated germanium, *Phys. Chem. Chem. Phys.* (2022).
- [41] W. Sah, H. Tsai, S. Lee, Physical and electronic structure of amorphous silicon carbon hydrogen alloy, *Appl. Phys. Lett.* 54 (7) (1989) 617–619, doi:10.1063/1.100896.
- [42] S.-Y. Lien, K.-W. Weng, J.-J. Huang, C.-H. Hsu, C.-T. Shen, C.-C. Wang, Y.-S. Lin, D.-S. Wu, D.C. Wu, Influence of CH<sub>4</sub> flow rate on properties of HF-PECVD a-sic films and solar cell application, *Curr. Appl Phys.* 11 (1) (2011) S21–S24, doi:10.1016/j.cap.2010.11.009.
- [43] M. Fathallah, R. Gharbi, G. Crovini, F. Demichelis, F. Giorgis, C. Pirri, E. Tresso, P. Rava, Light-soaking in a-sic:h films grown by PECVD in undiluted and hydrogen diluted sih<sub>4</sub> + CH<sub>4</sub> gas mixtures, *J. Non Cryst. Solids* 198–200 (1996) 490–494 (PART 1), doi:10.1016/0022-3093(95)00754-7.
- [44] H. Tran, W. Du, S.A. Ghetmiri, A. Mosleh, G. Sun, R.A. Soref, J. Margetis, J. Tolle, B. Li, H.A. Naseem, S.Q. Yu, Systematic study of  $Ge_{1-x}Sn_x$  absorption coefficient and refractive index for the device applications of si-based optoelectronics, *J. Appl. Phys.* 119 (10) (2016) 103106, doi:10.1063/1.4943652.
- [45] TETRAMETHYLITIN, 99% | gelest, inc.
- [46] B. Ruscic, Active thermochemical tables: sequential bond dissociation enthalpies of methane, ethane, and methanol and the related thermochemistry, *J. Phys. Chem. A* 119 (28) (2015) 7810–7837, doi:10.1021/acs.jpca.5b01346.
- [47] Y. Luo, Handbook of bond dissociation energies in organic compounds, *J. Am. Chem. Soc.* 126 (3) (2004) 982–982, doi:10.1021/ja0336224.
- [48] M. Decouzon, J. Gal, J. Gayraud, P. Maria, G. Vaglio, P. Volpe, Fourier transform-ion cyclotron resonance study of the gas-phase acidities of germane and methylgermane; bond dissociation energy of germane, *J. Am. Soc. Mass Spectrom.* 4 (1993) 54–57.